Benchmarking of Molecular Dynamics Force Fields for Solid-Liquid and Solid-Solid Phase Transitions in Alkanes

Stephen A. Burrows,[†] Ivan Korotkin,[‡] Stoyan K. Smoukov,[*,†] Edo Boek,[†] and Sergey Karabasov[¶]

[†]*Chemical Engineering and Renewable Energy, School of Engineering and Materials Science, Queen Mary University of London, London, E1 4NS, UK*

[‡]*Mathematical Sciences, University of Southampton, Southampton, SO17 1BJ, UK*

[¶]*Aerospace Engineering and Fluid Mechanics, School of Engineering and Materials Science, Queen Mary University of London, London, E1 4NS, UK*

E-mail: s.smoukov@qmul.ac.uk

Phone: +44 (0)20 7882 5305

Abstract

Accurate prediction of alkane phase transitions involving solids are needed to prevent catastrophic pipeline blockages, improve lubrication formulations, smart insulation and energy storage, and bring fundamental understanding to processes such as artificial morphogenesis. However, simulation of these transitions is challenging and therefore often omitted in force field development. Here we perform a series of benchmarks on seven representative molecular dynamics models (TraPPE, PYS, CHARMM36, L-OPLS, COMPASS, Williams, and the newly optimized Williams 7B), comparing with experimental data for liquid properties, liquid-solid and solid-solid phase transitions of two prototypical alkanes—n-pentadecane (C_{15}) and n-hexadecane (C_{16}). We find existing models overestimate the melting points by up to 34 K, with PYS and Williams 7B yielding the most accurate results deviating only 2 K and 3 K from experiment. We specially design order parameters to identify crystal-rotator phase transitions in alkanes. United-atom models could only produce a rotator phase with complete rotational disorder, whereas all-atom models using a 12-6 Lennard-Jones potential show no rotator phase even when superheated above the melting point. In contrast, Williams (Buckingham potential) and COMPASS (9-6 Lennard-Jones) reproduce the crystal-to-rotator phase transition, with the optimized Williams 7B model having the most accurate crystal-rotator transition temperature of C_{15}.

Introduction

Solid n-alkanes demonstrate a rich variety of crystal structures and rotationally disordered 'rotator' (plastic crystal) phases, with a complex dependence on chain length.[1–3] In the rotator phase with slightly higher unit cell volumes, the molecules remain straight (all-trans) and packed in lamellar layers with crystalline positional order, but with partial or full rotational freedom around the long molecular axis, disrupting the long-range orientational order. Phase transitions of alkanes are crucial to the function of many industrial products, and are closely related to phase changes of lipid membranes in living cells.[4] Phase change

materials for energy storage are a prime application, where alkanes are an attractive choice due to their high enthalpy of fusion, stability and lack of corrosivity.[5] However, challenges are presented by the significant volume change upon solidification or melting,[6] and the presence of the rotator phases, which increase the temperature range needed to utilize the entire latent heat capacity of the alkane.[7]

Crystallization of n-alkanes/waxes in crude oils is a major problem in the hydrocarbon recovery industry.[8] Under geological reservoir conditions of elevated temperature and pressure, most n-alkanes in crude oils are in the liquid state. As hydrocarbons are recovered and brought to the seafloor surface, the temperature change induces liquid-solid phase transitions, leading to deposition of solid wax in the pipelines. As an alternative to mechanical removal, significant research efforts have been directed to the physico-chemical inhibition of wax formation by the development of wax inhibitor additives.[9] As experiments covering a wide temperature and pressure range are difficult, computer simulation plays an important role in discovering the molecular mechanisms underlying wax crystal nucleation, growth and inhibition.[10,11]

When connected to a hydrophilic fragment, alkanes create amphiphilic surface-active agents (surfactants) widely used in multi-phase production processes—including foods,[12] detergents,[13] and paints.[14] The cellular membranes of all living things contain phospholipids,[15] natural surfactants, where gel-liquid phase transitions of their alkyl tails influence the mechanical properties, membrane permeability and lipid diffusion.[16]

Furthermore, surfactants at the alkane-water interface are known to nucleate rotator phases in alkane droplets, even when the phase is not thermodynamically stable in the bulk alkane.[17] This ordered layer introduces elastic properties to the droplet surface, and is capable of controlling shape and size of the droplets.[18] Droplets of oil can transform upon cooling into non-spherical geometric shapes including icosahedrons and polygonal platelets,[19,20] as well as droplets spontaneously splitting up into smaller ones only from small temperature fluctuations.[21,22] These processes of artificial morphogenesis promise sustainable manufac-

turing growing non-spherical particle shapes and sizes without waste, since reactive monomer oils have also been transformed this way and polymerized completely by UV irradiation.[23,24] Some of these shape changes can be partly modeled by considering their topology and the thermodynamics of rotator phase nucleation and growth,[25,26] but the molecular mechanisms are being debated. Experiments using organic surfactants suggest that rotator phase multilayers mediate the artificial morphogenesis process,[27] while reports with the ionic surfactant C_{18}TAB limit the frozen interface to a monolayer.[24,28]

To reproduce rotator phase transitions at the molecular level, models are needed that can reliably reproduce liquid-solid and solid-solid phase transitions. Such simulations would be able to model the crystallization of rotator phases in polythenes with their associated nucleation barrier in addition to perfect crystals.[29] They could also describe anisotropic thermal diffusivity in these polymers or their melts[30] advancing understanding in injection molding. Current extraction of oils and gas from kerogen in shale currently leaves up to 35% of methane and most liquefiable oil trapped, because of a lack of understanding of the energy barriers and interactions at liquid and solid interfaces.[31] Molecular Dynamics (MD) simulations are needed to complement experimental efforts to understand the melting and replacement of confined wax by water which is often both non-intuitive and essential for catalysed industrial synthesis reactions.[32]

MD simulation of solid-liquid and solid-solid phase transitions presents unique challenges, distinct from those of modeling isotropic liquid and vapor. Since solid n-alkanes demonstrate polymorphism[33] and rotator phases which are stable over a narrow temperature window,[2] it is a great challenge for an MD force field to predict the correct equilibrium phase due to subtle differences in free energy between them. This can be particularly problematic if the desired temperature for the simulation is close to a phase transition temperature. We compare the performance of a representative set of seven of the most widely used force fields to simulate these phase transitions. We aim to determine how the key characteristics of MD force fields, such as the pair potential form or level of coarse-graining, affect their suitability

for modeling liquid-solid and solid-solid phase transitions in n-alkanes. In doing so, we hope to assist researchers in choosing a suitable force field based on the compromise between accuracy and computational cost.

In classical MD force fields, the 12-6 Lennard-Jones (LJ) potential is the most common model for intermolecular interactions between atoms. However, molecular dynamics studies of $C_{23}H_{48}$ by Wentzel and Milner[34,35] showed that the Williams force field,[36] which uses Buckingham pair potentials, reproduced the correct crystal to rotator phase transition whereas the OPLS-AA force field did not. Since the Buckingham potential has an exponential repulsive term which is softer than the rapidly diverging $\sim r^{-12}$ term in the 12-6 LJ potential, it has been suggested that reducing the exponent, for example to $\sim r^{-9}$, can yield a more physically realistic potential.[37,38] There are known downsides to this approach, as Galliéro et al. found that changing this exponent (positively or negatively) worsened reproduction of viscosity and pressure for many simple liquids including ethane, even after optimization of the potential parameters.[39]

United-atom models of n-alkanes, in which CH_2 and CH_3 groups are treated as a single pseudoatom or bead, have been found to form a rotationally disordered solid phase even at temperatures far below the melting point.[40] Despite this limitation, united-atom models are routinely used in simulations of alkane or lipid phase change due to their computational efficiency.[41–43] Larger gains in computational performance can be obtained by further coarse-graining, such as the MARTINI force field model of polyethylene[44] in which four CH_x groups are represented by a single bead. In this model, the angle between adjacent bonds is 180°, so the atoms are colinear at the minimum potential energy and the molecules are essentially rod-like in the solid phase. Therefore it is not possible for this type of model to differentiate crystal and rotator phases, as the rotational orientation of the alkane molecule about its long axis is not well defined.

The dihedral (torsion) potentials of a force field determine the relative energy of different conformers and are key to accurately reproducing the melting point of solids. They are

typically fit to quantum chemistry calculations performed on individual molecules *in vacuo*, which can be a source of inaccuracy for condensed phases. As n-alkane molecules transition into straight all-trans conformers upon freezing, the dihedral potential influences the energy difference between the solid and liquid phases and is therefore a significant factor in determining the melting point of an n-alkane force field. Siu et al. optimized the OPLS-AA force field[45,46] for long hydrocarbons, and were able to improve reproduction of the melting point via refitting of the torsion potential and refinement of the partial charges. Improvements in the reproduction of viscosity and self-diffusion coefficients have also been achieved by optimizing only the torsion potential in alkane force fields.[47]

In the remainder of this work, we describe an approach under which we can produce one-to-one comparisons of different molecular dynamics models by reproducing various aspects of alkane phase transitions, creating a benchmark by which the performance of present and future models can be judged. We summarize the force fields chosen for comparison and their fundamental differences. Following, we present the challenges we solve to create consistent and reproducible comparisons, including the choice of system to measure melting points, tackling homogeneous nucleation, and the choice of order parameters to differentiate between crystal and rotator phases. Then we present the results of the comparison, the methods that are best able to reproduce the experimental results, as well as a newly optimized model to yield improved prediction of transition properties. We illustrate the approach with both an odd-numbered alkane, n-pentadecane (abbreviated C_{15}), and an even one, n-hexadecane (C_{16}), which have different crystal structures.

Simulation Methods

Force Fields Chosen for Comparison

Simulations of solid-liquid phase change typically require long time scales due to the energy barrier associated with nucleation events, so computational efficiency is a priority. Therefore

we choose to use classical non-reactive force fields compatible with the GROMACS molecular dynamics software,[48] which is used for all simulations in this work. In these models, covalent bonds between pairs of atoms are defined in advance and cannot be broken during the simulation.

A selection of force fields was chosen to include coarse-grained (MARTINI), united-atom (TraPPE and PYS) and all-atom representations (CHARMM36, L-OPLS, COMPASS, Williams) with different pair potential forms including 12-6 LJ, 9-6 LJ, and Buckingham. A brief summary of these force fields is given in Table 1, which specifies the main characteristics of each force field. A review of these force fields is provided in the Supporting Information, including a description of bond, angle and dihedral potential forms. The GROMACS-compatible parameter files are also provided as Supporting Information.

Table 1: Summary of the force fields used in this work.

Force field	Atom types	Pair potential	Constraints	1–4 interactions	Charges
TraPPE[49]	United-atom	12-6 LJ	All bonds	No	No
PYS[29,50]	United-atom	12-6 LJ	None	No	No
MARTINI[44,51]	Coarse-grained	12-6 LJ	None	No	No
CHARMM36[52]	All-atom	12-6 LJ	C-H bonds	Yes[a]	Yes
L-OPLS[45]	All-atom	12-6 LJ	C-H bonds	Half ($\epsilon^{ij}_{1-4} = \epsilon^{ij}/2$)	Yes
COMPASS-gmx[37]	All-atom	9-6 LJ	C-H bonds[b]	Full	Yes
Williams[36]	All-atom	Buckingham	C-H bonds[b]	No	No

[a] 1–4 parameters for CHARMM36 are given in the pairtypes section of the ffnonbonded.itp file.
[b] Previously these force fields have been used with harmonic C-H bonds, but we constrain them consistently across all force fields.

Simulation Settings

Firstly we outline the settings common to all simulations in this work. Table 2 contains values for the pair potential cut-off parameters and time step for each force field. All simulations were performed using GROMACS[48] version 2016.3 or newer, with the specific version used for each simulation given in the Supporting Information. Periodic boundary conditions were always used. The Bussi-Donadio-Parrinello velocity rescaling thermostat[53] (denoted in GROMACS as v-rescale) with a time constant of 0.1 ps was used to control the temperature.

The Parrinello-Rahman barostat[54] was used to control the pressure, with a time constant of 4 ps. The initial value of 2 ps was found to result in large density fluctuations, especially with L-OPLS, and 4 ps is consistent with that used in the L-OPLS force field development.[45] The compressibility constant of the barostat was set to 5×10^{-5} bar^{-1} for all degrees of freedom. The pressure was fixed to 1 bar, and the temperature was varied as described in this section for each simulation type. For the COMPASS-gmx and Williams force fields, the pair potentials were implemented in tabulated form, with an r spacing of 0.002 nm. A long-range dispersion correction was applied to the energy and pressure (using the GROMACS option DispCorr = EnerPres) for all force fields except for CHARMM36. Properties of the CHARMM36 force field are reported both with and without this correction, because the dispersion correction is only recommended for certain systems when using CHARMM36.[52]

Table 2: Force field parameters which define the pair potential cut-off, long range dispersion correction and time step.

Force field	r_{switch} [a] [nm]	r_{cut} [nm]	Disp. corr. [b]	Time step [fs]
TraPPE[49]	-	1.4	Yes	2
PYS[29,50]	-	1.0	Yes	2
MARTINI[44,51]	-	1.1	Yes	10
CHARMM36[52]	1.0	1.2	No	1
L-OPLS[45]	1.1	1.3	Yes	2
COMPASS-gmx[37]	-	1.0	Yes	1
Williams[36]	-	1.0	Yes	1

[a] r_{switch} is the radius at which to start applying the GROMACS force-switch function which smoothly reduces the force to zero at the cut-off r_{cut}.

[b] 'Yes' indicates the long range correction to energy and pressure is used by setting DispCorr = EnerPres in GROMACS.

Liquid Properties

It is useful to measure some properties of the liquid phase as these may be relevant to multiphase systems, specifically the liquid-solid phase changes which are studied in this work. For example, the rate of crystal growth may be diffusion-limited, in which case the self-diffusion coefficient is a relevant property. The density and self-diffusion coefficient were

obtained for each force field and for C_8, C_{15} and C_{16} at 298 K and 1 bar. The inclusion of C_8 was to provide more information as to how these properties scale with chain length.

The properties were measured by averaging the results from five independent 4 ns trajectories, for a total time of 20 ns. Before each of these, a 2 ns equilibration was performed using randomized starting velocities sampled from the Maxwell distribution, using the gen-vel option in GROMACS. This is to introduce more independence between runs which would otherwise be correlated due to having the same starting configuration. To estimate the uncertainty of these measurements, the trajectory was further subdivided into 1 ns blocks and the properties were measured for each block. The standard deviation of these individual measurements is then calculated using $\sigma_b^2 = \sum_{i=1}^{N_b} \left(D_i - \langle D \rangle\right)^2 / (N_b - 1)$, where D_i is the self-diffusion coefficient measured from block i and N_b is the total number of blocks. Then the standard deviation of the overall average is calculated as $\sigma = \sigma_b / \sqrt{N_b}$, and the uncertainty reported is two standard deviations. The self-diffusion coefficient is measured using the mean squared displacement method, and an approximate finite-size correction is applied using the formula by Yeh and Hummer[55] (Eq. 14 in their work). In this version of the finite-size correction, the viscosity is computed implicitly using the hydrodynamic radius and the Stokes-Einstein relation. In the Supporting Information, the self-diffusion coefficient is computed for a range of system sizes from 128 to 2048 molecules, finding that no significant finite-size effect remained after applying the Yeh-Hummer correction. The stick-limit hydrodynamic radius needed for this correction is approximately 0.17 nm for n-alkanes.[56]

Conformational Change During Liquid Cooling and Nucleation

A cooling and heating cycle was performed on the equilibrated liquid systems resulting from the liquid properties study. The trans fraction of all C-C-C-C dihedral angles (f_{trans}) was chosen to serve as the order parameter to detect liquid-solid phase change, and was computed for each trajectory frame. For an ideal crystal f_{trans} will be unity as the molecules are in all-trans conformation, but in the liquid phase values of 0.6-0.8 were observed. A trans dihedral

is defined as the dihedral angle being in the range $120^\circ < \phi < 240^\circ$, with the definition of ϕ shown in Fig. S1 of the Supporting Information.

To define the cooling-heating cycle, the system begins in the liquid phase at $T_m + 50$ K, where T_m is the experimentally observed melting point, and is cooled linearly to $T_m - 50$ K over a period of 50 ns. The system was then heated back to $T_m + 50$ K over a further 50 ns, to complete a symmetric cycle with total length 100 ns. The large range of ± 50 K was chosen to account for potential errors in the melting points of the models and for supercooling and superheating effects.

In the liquid phase, f_{trans} gradually increased as the temperature decreased, and could be modeled well as a linear function of temperature. At the point nucleation occurs, f_{trans} rapidly increases during the freezing process, so there is a discontinuity in the gradient of f_{trans} which can be used to identify nucleation. By fitting a piecewise linear function to f_{trans} (i.e. a series of straight line segments), the discontinuities in the gradient could be identified as the points at which the linear segments connect. The first line segment corresponds to the liquid phase, so the end of this segment is used to identify the nucleation point. A visual inspection of the trajectory was used to confirm the formation of solid. The number of line segments in the piecewise linear fit was increased until the root mean square deviation from the computed f_{trans} was $< 0.5 \times 10^{-3}$ (dimensionless) in all cases. This is because f_{trans} may evolve with time in a complex way once the system is mostly solidified, so increasing the number of line segments helps achieve a good fit to f_{trans} for the entire cooling-heating cycle.

Classical nucleation theory (CNT) was applied to molecular dynamics simulations of C_8 and C_{20} nucleation by Yi and Rutledge,[42,57] using the PYS force field. In CNT, the overall nucleation rate per unit volume and per unit time follows an Arrhenius law

$$J = J_0 \mathrm{e}^{-\Delta G^*/k_B T} \ , \tag{1}$$

where J_0 is the barrier-free nucleation rate related to the frequency of transport of single

molecules at the nucleus-matrix interface. ΔG^* is the free energy of formation of a solid nucleus of a critical size,[58] beyond which growth of the nucleus becomes thermodynamically favorable (corresponding to a decrease in total free energy). For a system with volume V, the nucleation rate per unit time is given by $\lambda = JV$, and the number of supercritical nuclei formed in a time interval of length t can be modeled by a Poisson distribution $P[k]$ with parameter $\mu = \lambda t$.[59]

$$P[k] = \frac{\mu^k \mathrm{e}^{-\mu}}{k!} \ , \tag{2}$$

where $P[k]$ is the probability of k supercritical nuclei forming in time t. As the temperature is varying in our simulations, the nucleation rate λ also varies and therefore a nonhomogeneous Poisson process is used in which the Poisson parameter μ is given by

$$\mu = \int_0^t \lambda(\tau) \mathrm{d}\tau, \tag{3}$$

which is the average value of λ over the time period 0 to t, multiplied by t. Yi and Rutledge report the critical free energy in the form $\Delta G^*/k_B T$ for several values of the dimensionless supercooling $(T_m - T)/T_m$. In the Supporting Information, their reported data is used to estimate the probability of a supercritical nucleus forming for the temperature cycle specified above ($T_m \pm 50$ K), using the PYS force field and C_{16}. The results suggest the nucleation probability is only $\approx 10\%$, when the above temperature range is used, increasing to 32% if the temperature interval is shifted down by 10 K (starting at T_m+40 K, cooling to T_m−60 K), and 60% if shifted down by 20 K. Therefore these lower temperature ranges were considered in the event that nucleation was not observed for certain force fields.

Melting Point Determination Using Interface Method

The melting point is a key property for assessing a force field's suitability for solid-liquid systems. If it is inaccurate, the force field may predict phase transitions which would not occur in reality. Many methods have been suggested to compute the melting point from

molecular dynamics,[60] and we choose an interface-based method which has been successfully applied to n-alkanes previously.[42] An initial configuration is prepared with both solid and liquid phases present, which is evolved at a constant temperature to assess whether that temperature is above or below the melting point. If it is below the melting point, we expect the solid fraction of the system to increase and therefore the density to also increase, with the opposite if the temperature is above the melting point. A planar interface as shown in Figure 1 is used, as the solid phase can grow or shrink without a change in interfacial area, so the process is driven primarily by the free energy difference between the solid and liquid phases rather than minimization of the surface free energy. The initial temperature scan for each configuration was performed in 4 K increments to cover a wide range, followed by 2 K and finally 1 K to refine the melting point further.

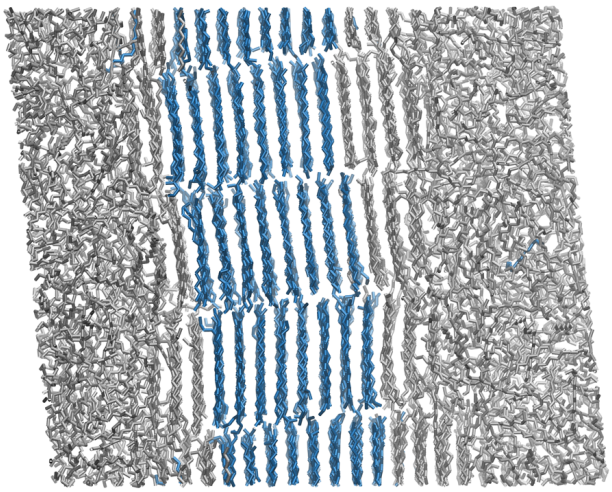

Figure 1: Planar interface configuration used in the melting point study, rendered using VMD.[61] The molecules colored in blue are those with the potential well depth doubled to artificially raise their melting point during the equilibration phase of the simulation.

To prepare the planar interface, the method of Bai and Li[62] is used, which was applied to create a solid-liquid interface of C_8 by Yi and Rutledge.[42] In this method, a large enough supercell of a perfect crystal is defined. Then the interaction strength for a subset of the molecules forming a slab in middle of the system is increased, which allows this region to remain solid whilst the system is heated above its usual melting point to melt the rest.

The increased attraction is achieved by doubling the well-depth parameter ϵ in the LJ or Buckingham potentials. An NVT simulation of 4 ns at 360 K was sufficient to completely melt all but the defined solid slab, resulting in the configuration shown in Figure 1. The dimensions of the supercells used to define the initial coordinates of the system are provided in Table 3. Molecules spanning one third of the simulation domain along the a lattice direction were kept frozen, and the solid completely spans the b and c directions (with periodic boundary conditions). For this reason, fully anisotropic pressure coupling was used to relieve any shear stresses, and the off-diagonal compressibility values were set equal to the diagonal ones at 5×10^{-5} bar^{-1}.

Table 3: System sizes defined by initial crystal supercells and the number of molecules used for each simulation type.

Molecule	System	Supercell	Num. molecules
C_{15}	Liquid properties	N/A	1024
	Interface (melting)	$20 \times 10 \times 2$	1600[a]
	Crystal	$15 \times 10 \times 3$	1800[a]
C_{16}	Liquid properties	N/A	1024
	Interface (melting)	$24 \times 16 \times 4$	1536
	Crystal	$18 \times 18 \times 4$	1296
C_8	Liquid properties	N/A	2048

[a]The unit cell of C_{15} contains four molecules. Unit cells of C_{15} and C_{16} are provided in the Supporting Information.

Simulation of Crystal-Rotator Phase Transitions

Simulations were performed starting from the experimentally observed crystal structures of C_{15} and C_{16}. The size of the supercells used are given in Table 3. The purpose of these simulations is to observe the solid structure over a heating and cooling cycle, as characterized by order parameters, and compare this to experimentally observed structures and solid-solid phase transition temperatures. Temperature ranges of 270–310 K and 280–320 K were used for C_{15} and C_{16} respectively, and the temperature is varied linearly during the heating and cooling segments which are 20 ns each (2 K/ns heating and cooling rate). This

temperature profile is plotted alongside the order parameters for clarity. To ensure stability of the Parinello-Rahman pressure coupling, it was necessary to reduce the parameter nstPcouple to 2, so the box vectors are updated every other time step.

Defining Order Parameters

To detect solid-solid phase change and to facilitate comparison to experimentally determined transition temperatures, order parameters are needed to differentiate between states of varying rotational order. Firstly, the orientation of each molecule is defined by computing the principal components of the coordinates of its atoms. The first principal component vector, $\boldsymbol{p}_1$, aligns with the long axis of the n-alkane molecule as to minimize the average squared distance between $\boldsymbol{p}_1$ and the atoms. The second component, $\boldsymbol{p}_2$, defines a best-fit plane containing $\boldsymbol{p}_1$ and $\boldsymbol{p}_2$ such that the carbon atoms lie approximately in this plane. Therefore $\boldsymbol{p}_2$ is used to define the rotational orientation of the alkane molecules about their long axes, with the angle denoted ψ in Figure 2. We define continuous order parameters which are periodic functions of ψ, as these can also provide a measure of thermal disorder in addition to determining the overall structure. It should be noted that the angle ψ, and therefore the order parameters, are defined relative to a reference axis denoted $\boldsymbol{a}_{\text{ref}}$ in Figure 2, which is parallel to the $\boldsymbol{a}$ lattice direction of the initial crystal. In principle, there are three possible values which the reference axis can take on a pseudohexagonal lattice, and the order parameters should be computed for each possible choice to determine the overall orientation of the crystal. However, we do not observe solid-solid phase change corresponding to three-fold rotation about the z axis, so the original orientation of the crystal is maintained.

Firstly we introduce an order parameter to measure the level of rotational disorder. This parameter should assign a value of unity in the case where all orientations are equally probable (maximum disorder). This allows us to detect crystal-rotator phase transition, and also distinguish between the first rotator phase $\mathrm{R_I}$, in which the molecules still demonstrate preferential orientations, and the second rotator phase $\mathrm{R_{II}}$, a hexagonal phase in which the

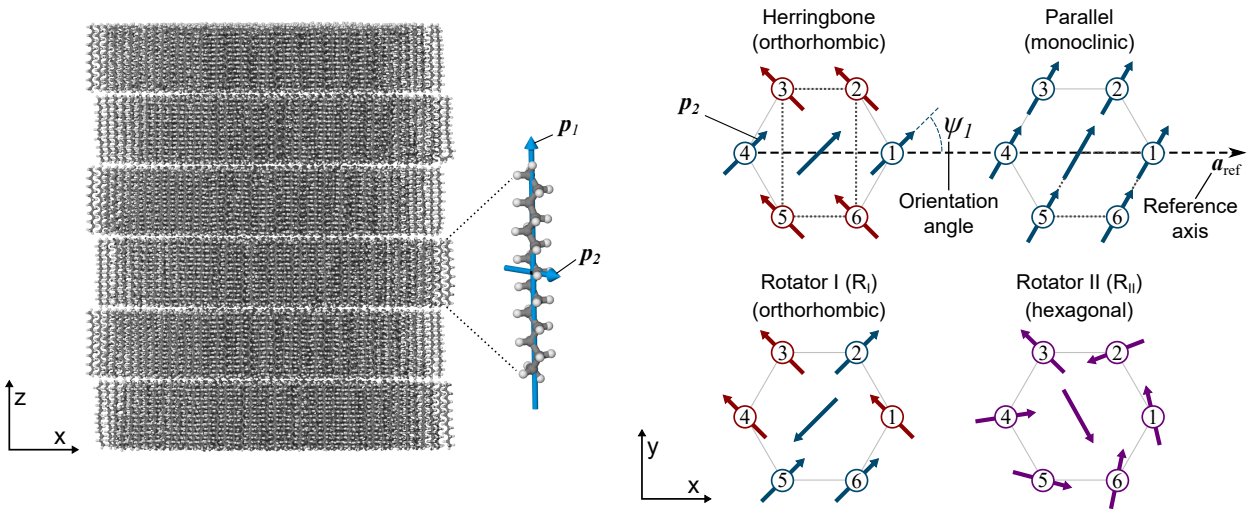

Figure 2: Illustration of how the principal components of the atomic coordinates of an n-alkane molecule can define its orientation. The second principal component, $\boldsymbol{p}_2$, defines the rotation of the molecule about its long axis and lies in the x-y plane. The pattern of $\boldsymbol{p}_2$ orientations is shown for two common crystalline arrangements (herringbone and parallel), and the rotator phase $\mathrm{R_I}$ (in which molecules undergo random rotations of $\pm 90°$) and $\mathrm{R_{II}}$ (near-complete rotational disorder).[34]

molecules approach complete rotational disorder.[63] For this purpose we calculate an order parameter Γ_i by a sum over all six nearest-neighbors of molecule i within a layer,

$$\Gamma_i = \frac{1}{6}\sum_{j=1}^{6}\left[1 - \cos\left(4\left(\psi_i - \psi_j\right)\right)\right] \ , \tag{4}$$

which is averaged over all N molecules to obtain $\Gamma = \frac{1}{N}\sum_{i=1}^{N}\Gamma_i$. If all neighboring pairs i and j are all exactly parallel or perpendicular, that is if $\psi_i - \psi_j = m90°$ where m is an integer, then Γ will be zero. If the orientation of the molecules is completely random Γ will equal unity, because the cosine part of the function will have zero average. Although this function was found to work well for the phases observed, it is not completely general, and can average > 1 in some cases. Therefore a complementary parameter was defined by creating a histogram of the orientation angles, with bin size 5°, and normalizing it to give a probability distribution $P(\psi_k)$ where k is the index of the histogram bin. The normalized

entropy of this distribution can then be computed as

$$S^R = -\frac{1}{\ln n_b} \sum_{k=1}^{n_b} P(\psi_k) \ln \left(P(\psi_k) \right) \ , \tag{5}$$

where n_b is the number of histogram bins. S^R has a value between 0 and 1, with 1 corresponding to complete rotational disorder, so we use it as an orientational order parameter.

We also define order parameters that are maximized at perfect crystal arrangements and quantify the amount of disorder away from them. The experimentally observed orthorhombic structure of C_{15} has herringbone rotational order of the $\boldsymbol{p}_2$ vectors, however a monoclinic phase with parallel order has also been observed in simulations.[34] These two types of rotational order are shown in Figure 2 (top right). Therefore we define an order parameter to differentiate these two structures.

The parallel (P_{ij}) and herringbone (H_{ij}) order parameters below are both derived from the following pairwise function

$$F_{ij} = \cos \left[2 \left(\psi_i - \tfrac{\pi}{4} \right) \right] \cos \left[2 \left(\psi_j - \tfrac{\pi}{4} \right) \right] = \sin \left(2\psi_i \right) \sin \left(2\psi_j \right) \ , \tag{6}$$

where the cosine form emphasizes that $\psi = \frac{\pi}{4}$ or 45° is the first maximum of the function, but the sine form is more concise. When a neighboring pair of molecules i and j are parallel and aligned at 45°, 135°, 225° and 315° with respect to the reference axis, $F_{ij} = 1$, indicating parallel order. If the molecules are perpendicular instead, but still aligned to one of these four preferential directions, then $F_{ij} = -1$, which indicates herringbone order. The computation of F_{ij} for a neighboring pair of molecules is illustrated in Figure 3. The parallel order parameter P_{ij} and herringbone order parameter H_{ij} are then taken as the positive and negative component of F_{ij} respectively.

$$P_{ij} = \begin{cases} F_{ij}, & \text{if } F_{ij} > 0 \\ 0, & \text{otherwise} \end{cases} \qquad H_{ij} = \begin{cases} -F_{ij}, & \text{if } F_{ij} < 0 \\ 0, & \text{otherwise.} \end{cases} \tag{7}$$

It should be noted that P_{ij} is not only a measure of how parallel the orientations of i and j are, but a combined measure of their parallelism and alignment to the four diagonal directions. For each molecule, the six nearest neighbors within the layer are determined based on the distance between their centers of mass. P_{ij} and H_{ij} are computed for each neighboring pair i and j, except for the two neighbors which are in the same row (those numbered 1 and 4 in Fig. 2), because these two will be parallel regardless of whether there is herringbone or parallel order. Averaging of the order parameters is performed in two stages. For each molecule i, the order parameters are averaged over its neighbors to obtain $P_i = \frac{1}{4}\sum_{j=2,3,5,6} P_{ij}$ and $H_i = \frac{1}{4}\sum_{j=2,3,5,6} H_{ij}$, where the sum over j refers to the sum over those neighbors (2, 3, 5 and 6) in Figure 2. Having computed the order parameter for each molecule, these are averaged over the entire system, obtaining $P = \frac{1}{N}\sum_{i=1}^{N} P_i$ and $H = \frac{1}{N}\sum_{i=1}^{N} H_i$ for a system of N molecules.

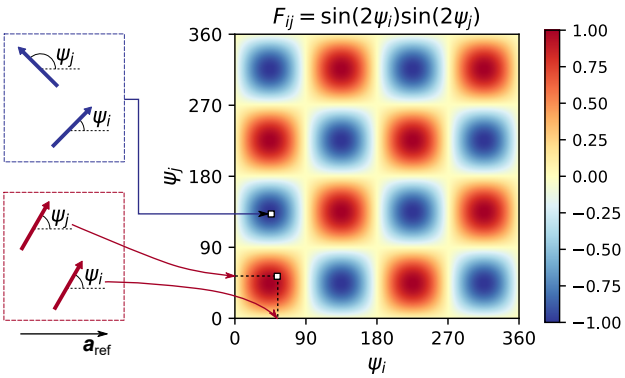

Figure 3: Pairwise order parameter F_{ij}, computed for adjacent pairs of molecules i and j, to differentiate herringbone and parallel ordering in n-alkane crystal layers. The color denotes the value of F_{ij} according to the color bar (right side), with positive (red) values and negative (blue) values corresponding to parallel and herringbone order respectively.

Optimization of a Williams Potential

Initial simulations of liquid C_{15} and C_{16} were performed using the Williams Buckingham potential parameter set 7.[36] This parameter set was created by fitting to data for non-aromatic hydrocarbons, including the lattice constants and heats of sublimation of C_5, C_6

and C_8. Tests found that the melting point was sensitive to the dihedral potential, and that the potential given by Tu, Tobias and Klein[64] yielded a quite accurate value, deviating less than 10 K from experiment. This torsion potential was therefore used unmodified for all Williams potential simulations, and is given in Table 4. However, it was found that this version of the Williams potential slightly overestimated the density and significantly underestimated the self-diffusion coefficient by approximately 50% for C_{15} and C_{16}.

To explain why the self-diffusion coefficient may be too low, it was noted that Williams used very short potential cutoffs of 0.6, 0.55 and 0.5 nm for C-C, C-H and H-H interactions respectively in the fitting procedure. This was necessary with the lack of computational power available at the time, but is not consistent with modern force fields which typically truncate pair potentials at 1 nm or more to reduce the force discontinuity at the cutoff. This will introduce attractive forces which Williams did not consider. Therefore we derive an optimized force field designed to be used with a 1 nm cutoff and long range dispersion corrections to the energy and pressure. The goal of the optimization is to achieve a potential which maintains the strengths observed by Wentzel and Milner[35] for reproducing crystal-rotator phase transitions, but with a more accurate reproduction of liquid density and self-diffusion coefficient.

Williams chose an H-C-H angle of 106°, which differs from the tetrahedral angle of 109.5°. Therefore a geometry optimization was performed of C_8, in all-trans conformation, to obtain C-C-C and C-C-H valence angles which are exactly consistent with the H-C-H angle constrained to 106°. The B3LYP functional and aug-cc-pvtz basis set were used to perform this geometry optimization using NWChem[65] version 6.6.

The potential well depth was modified according to the algorithm described herein, and the density and self-diffusion coefficient were measured as a function of this change to determine an optimal value. We start with the Buckingham potential given in terms of the

energy well depth ϵ and the atomic separation at the energy minima R_0,

$$U_{\text{Buck}}(r) = \epsilon \left[\frac{6}{\alpha - 6} \exp\left(\alpha \left(1 - \frac{r}{R_0} \right) \right) - \frac{\alpha}{\alpha - 6} \left(\frac{R_0}{r} \right)^6 \right] \ . \tag{8}$$

Since there are three parameters in the Buckingham potential (α being an additional dimensionless parameter which can control the shape of the potential well), two additional constraints are needed to solve for the new potential parameters. The equilibrium distance R_0 was kept constant, as this is directly related to the interatomic spacing and therefore the lattice constants which Williams fit to experiment. Despite fixing R_0, a change in density will still be observed due to a change in magnitude of the attractive forces between atoms resulting from the change in ϵ. For the second constraint, the second derivative of the potential at the energy minima was fixed. This quantity is related to elastic constants which Williams also fit for certain molecules. Equating the second derivatives requires that

$$\left. \frac{\partial^2 U_{\text{Buck}}}{\partial r^2} \right|_{r=R_0} = \frac{6\epsilon_1\alpha_1(\alpha_1 - 7)}{R_0^2(\alpha_1 - 6)} = \frac{6\epsilon_2\alpha_2(\alpha_2 - 7)}{R_0^2(\alpha_2 - 6)} \ , \tag{9}$$

where subscript 1 denotes the original parameters and subscript 2 the new set of parameters. Since R_0 will be fixed and ϵ_2 will be varied systematically in the fitting procedure, α_2 is the parameter to be solved for, which results in the quadratic equation

$$-\epsilon_2(\alpha_1 - 6)\alpha_2^2 + \left[\epsilon_1\alpha_1(\alpha_1 - 7) + 7\epsilon_2(\alpha_1 - 6)\right]\alpha_2 - 6\epsilon_1\alpha_1(\alpha_1 - 7) = 0 \ . \tag{10}$$

This is solved to find the larger root such that $\alpha_2 > 7$, which ensures the potential has a positive second derivative at the energy minima. In practice, the value of α is usually in the range 12–15 for Buckingham potentials used for intermolecular interactions. In Figure 4, this method of adjusting ϵ is compared to a simple potential rescaling (multiplying the potential by a constant). In the results section, properties will be presented as a function of the change in ϵ for the C-C potential, which is denoted $\Delta\epsilon = \epsilon_2 - \epsilon_1$. For the C-H and H-H interactions,

ϵ is rescaled by the same factor as for C-C, for example $\Delta\epsilon_{CH} = \Delta\epsilon_{CC}\,(\epsilon_{CH}/\epsilon_{CC})$, and the updated value of α computed according to Eq. 10.

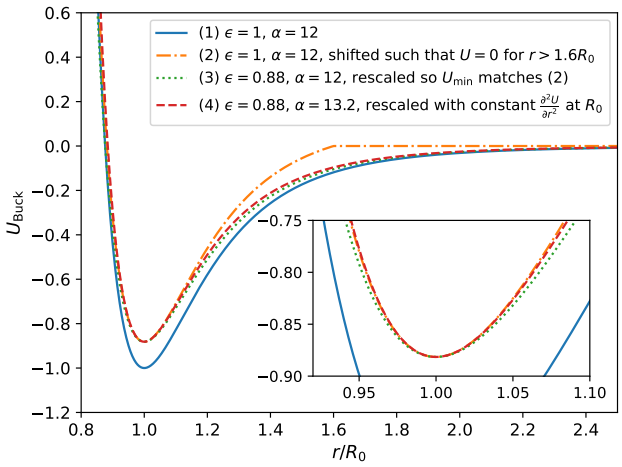

Figure 4: Illustration of three possible modifications which change the well depth of an example Buckingham potential. (1) A generic Buckingham potential with $R_0 = 1$, $\epsilon = 1$ and $\alpha = 12$. (2) The same potential shifted and truncated such that $U = 0$ for $r > 1.6R_0$. (3) A simple rescaling of the first potential, only changing ϵ, such that the minimum energy matches the shifted potential. (4) The method used in this work, in which the well depth of the potential is reduced whilst maintaining its second derivative at R_0, achieved by varying ϵ and α as described in the text.

Results

Optimized Williams Potential Parameters

Firstly the results of the Williams potential optimization are presented, as this defines the Williams 7B force field which is used in subsequent results. In Figure 5 the self-diffusion coefficient and density are plotted as a function of the change in C-C potential well depth, denoted $\Delta\epsilon$. Negative values of $\Delta\epsilon$ were used, which correspond to a reduction in the well depth and a weakening of the non-bonded interaction, leading to an increase in the self-diffusion coefficient and decrease in the density. The optimal value of $\Delta\epsilon$ was computed for each molecule and property, obtaining six values (3 molecules $\times$ 2 properties). An average of these was taken with all having an equal weighting, resulting in $\Delta\epsilon = -0.013$ kJ/mol.

Larger values of $\Delta\epsilon$ (approximately -0.024 kJ/mol) would be needed to reproduce the self-diffusion coefficient of C_{15} and C_{16}, but this would increase the error in the density and give poor results for shorter alkanes, as indicated by the results for C_8. If C_8 is excluded from the average, the optimal value would be $\Delta\epsilon = -0.016$ kJ/mol. The bonding potential parameters are given in Table 4. The Buckingham potential parameter set resulting from the optimization procedure ($\Delta\epsilon = -0.013$ kJ/mol), denoted Williams 7B, is shown in Table 5 alongside the original parameters.

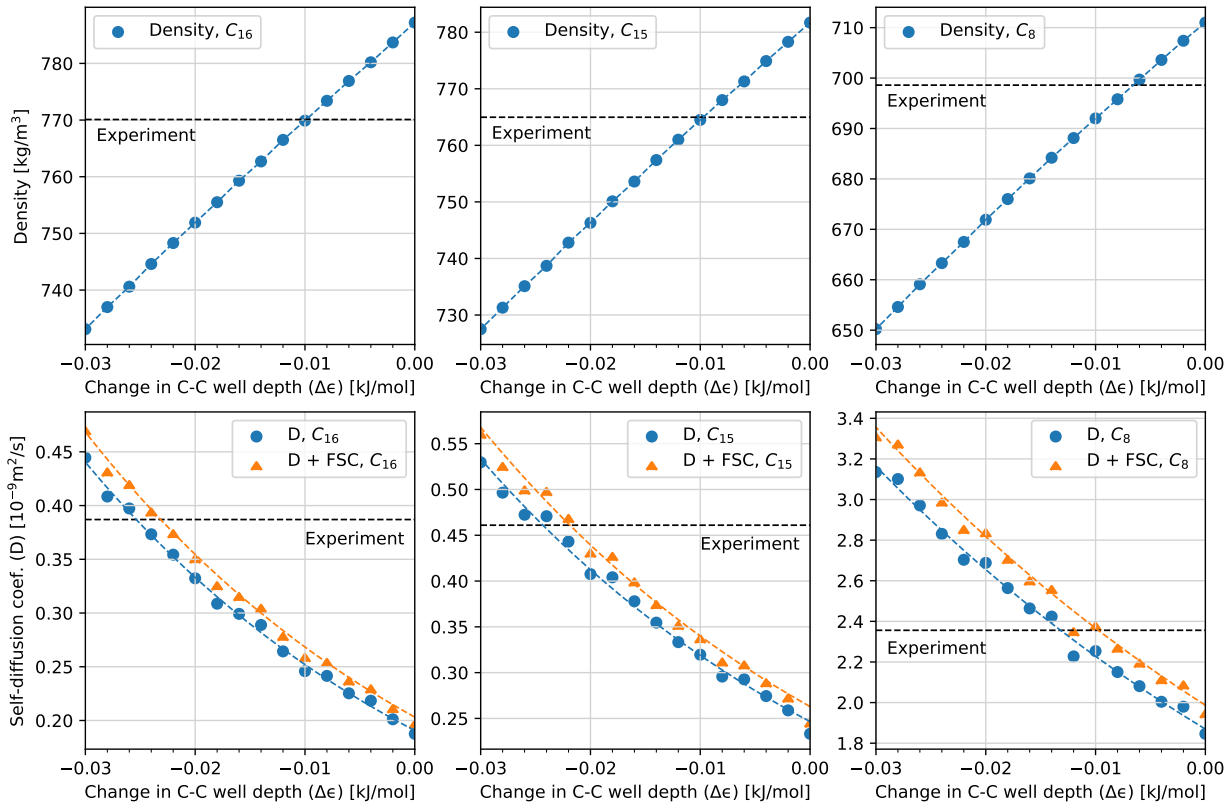

Figure 5: Variation of density and self-diffusion coefficient of C_{16}, C_{15} and C_8 as C-C Buckingham potential well depth (ϵ) is decreased. The value of ϵ for the C-H and H-H potentials is decreased proportionally. FSC denotes the addition of a finite size correction to the self-diffusion coefficient, for which an exponential model of $D = a_1 \exp(-a_2 \Delta\epsilon)$ was used to generate a least-squares best fit curve.

Table 4: Bonding potential parameters used for the Williams force fields. The θ_0 values are obtained from a geometry optimization described in the text. Harmonic coefficients k_b and k_θ are standard values also used by the L-OPLS and CHARMM36 force fields, and the dihedral potentials are from Tu et al.[64]

	Bond, $U_b(b) = \frac{1}{2}k_b(b - b_0)^2$	
	b_0 [nm]	k_b [kJ/mol]
C-C	0.153	224262.4
C-H	0.104	Constraint
	Angle, $U_\theta(\theta) = \frac{1}{2}k_\theta(\theta - \theta_0)^2$	
	θ_0 [degrees]	k_θ [kJ/mol/rad^2]
C-C-C	113.7	488.273
C-C-H	109.2	313.800
H-C-H	106.0	276.144
	Torsion potential $U_\phi = \sum_n k_n\,(1 + \cos(n\phi))$	
	n	k_n [kJ/mol]
C-C-C-C	1	0.9791
	2	0.4017
	3	1.7154
C-C-C-H	3	0.7406
H-C-C-H	3	0.6904

Table 5: Williams Buckingham potential parameters[a] used in this work.

Version[b]	Interaction	A [kJ/mol]	B [nm^{-1}]	C [nm^6·kJ/mol]
Williams 7	C-C	259.0×10^3	36.0	2.113×10^{-3}
	C-H	46.0×10^3	36.7	0.536×10^{-3}
	H-H	11.0×10^3	37.4	0.135×10^{-3}
Williams 7B	C-C	341.86×10^3	36.94	2.005×10^{-3}
(this work)	C-H	58.14×10^3	37.61	0.507×10^{-3}
	H-H	13.65×10^3	38.30	0.128×10^{-3}

[a] Parameters are given for the Buckingham potential form $U_{\text{Buck}}(r) = A\exp(-Br) - C/r^6$.
[b] Version 7 is from the original work of Williams,[36] version 7B was derived in this work and is designed to be used with a cutoff of 1 nm and long range dispersion correction to the energy and pressure.

Liquid Density and Self-Diffusion Coefficient

The measured density and self-diffusion coefficients for each force field are given in Table 6. We use the finite-size corrected value of the self-diffusion coefficient for comparison to experiment, which we simply denote D. The united-atom models overestimate D, although the PYS force field is within 8% for C_8 and approximately 25% for C_{15} and C_{16}. TraPPE had the largest deviation of all models, overestimating D by 84% for C_{16}. Other authors have found TraPPE underestimates alkane viscosity, which is to be expected according to the Stokes-Einstein relation between diffusion coefficient and viscosity. Saley Hamani et al. found TraPPE underestimated the viscosity of C_6-C_{12} mixtures with an average absolute deviation of 35%,[66] and Messerly et al. found TraPPE underestimated the viscosity of saturated liquid C_{16} by up to 55%, with the accuracy improving as temperature increased.[67] The all-atom force fields generally underestimate D, with the relative error increasing with the length of the alkane. CHARMM36 (without the long-range dispersion correction) gave the most accurate prediction of D, with a mean absolute deviation of 12.9%, followed by Williams 7B with 17.4%. The uncorrected value of the self-diffusion coefficient for the L-OPLS model of C_{15} was 0.299 10^{-9}m^2/s, which matches closely that reported in the L-OPLS publication for similar system sizes (comparing to Fig. 8 of Ref. 45). After applying the finite size correction to D, we obtain a slightly lower value than Siu et al. (0.319 vs 0.329 10^{-9}m^2/s). This can be attributed to the different method for the correction, with Siu et al. using an extrapolation method instead of the Yeh-Hummer[55] correction. The density of 763.59 kg/m^3 is also a close match to the L-OPLS publication. The optimization of the Williams potential reduced the mean absolute error of the density from 2.1% to 1.1%, and of D from 35.6% to 17.4%.

Computed Trans Dihedral Fractions and Nucleation Observations

The evolution of the trans dihedral fraction (C-C-C-C dihedrals) of C_{16} during the cooling-heating cycle is plotted in Figure 6, and the equivalent plots for C_{15} are given in the Sup-

Table 6: Measured density and self-diffusion coefficient at 298 K and 1 bar for C_8, C_{15} and C_{16} and all force fields.

Molecule	Force field	ρ [kg/m^3]	$D_{\mathrm{PBC}}{}^d$ [10^{-9}m^2/s]	D+FSC^d [10^{-9}m^2/s]
C_8	TraPPE	705.21 (± 0.08)	3.498 (± 0.077)	3.716 (± 0.082)
	PYS	691.88 (± 0.17)	2.395 (± 0.045)	2.544 (± 0.048)
	MARTINI	783.00 (± 0.05)	2.292 (± 0.046)	2.442 (± 0.049)
	CHARMM36	700.15 (± 0.11)	1.969 (± 0.034)	2.091 (± 0.036)
	CHARMM36 (no DC)[c]	677.57 (± 0.14)	2.612 (± 0.067)	2.772 (± 0.071)
	L-OPLS	694.27 (± 0.07)	1.873 (± 0.056)	1.989 (± 0.060)
	COMPASS-gmx	705.79 (± 0.09)	1.910 (± 0.028)	2.029 (± 0.030)
	Williams 7	711.04 (± 0.11)	1.891 (± 0.045)	2.010 (± 0.048)
	Williams 7B (this work)	686.05 (± 0.09)	2.342 (± 0.054)	2.487 (± 0.057)
	Experiment	698.4[a]	-	2.356[b]
C_{15}	TraPPE	775.74 (± 0.08)	0.827 (± 0.015)	0.882 (± 0.016)
	PYS	767.21 (± 0.27)	0.547 (± 0.018)	0.584 (± 0.019)
	CHARMM36	769.82 (± 0.10)	0.342 (± 0.010)	0.365 (± 0.011)
	CHARMM36 (no DC)[c]	750.97 (± 0.17)	0.479 (± 0.011)	0.510 (± 0.012)
	L-OPLS	763.59 (± 0.12)	0.299 (± 0.009)	0.319 (± 0.010)
	COMPASS-gmx	775.84 (± 0.13)	0.264 (± 0.012)	0.281 (± 0.013)
	Williams 7	781.81 (± 0.12)	0.240 (± 0.010)	0.256 (± 0.011)
	Williams 7B (this work)	759.08 (± 0.16)	0.346 (± 0.016)	0.369 (± 0.017)
	Experiment	764.9[a]	-	0.461[b]
C_{16}	TraPPE	781.22 (± 0.09)	0.667 (± 0.020)	0.711 (± 0.021)
	PYS	773.08 (± 0.17)	0.457 (± 0.014)	0.487 (± 0.015)
	MARTINI	825.13 (± 0.06)	0.581 (± 0.024)	0.620 (± 0.026)
	CHARMM36	775.18 (± 0.16)	0.283 (± 0.010)	0.301 (± 0.011)
	CHARMM36 (no DC)[c]	756.67 (± 0.12)	0.402 (± 0.009)	0.427 (± 0.009)
	L-OPLS	768.59 (± 0.08)	0.246 (± 0.008)	0.262 (± 0.009)
	COMPASS-gmx	781.33 (± 0.18)	0.209 (± 0.005)	0.222 (± 0.005)
	Williams 7	787.07 (± 0.18)	0.191 (± 0.004)	0.203 (± 0.004)
	Williams 7B (this work)	764.67 (± 0.10)	0.267 (± 0.005)	0.284 (± 0.006)
	Experiment	769.8[a]	-	0.387[b]

[a]Experimental densities are from Aucejo et al.[68] for C_8 and C_{16} (at 298.15 K), and from Daridon et al.[69] for C_{15} by a linear interpolation between 293.15 and 303.15 K.

[b]Experimental self-diffusion coefficients were taken from Tofts et al.[70]

[c]'no DC' denotes CHARMM36 values computed without the long range dispersion correction.

[d]D_{PBC} denotes the diffusion coefficient directly measured using the mean squared displacement method, and D+FSC after the finite size correction has been applied.

porting Information. The trans dihedral fraction at 298 K is labeled and varies from 0.632 (L-OPLS) to 0.745 (TraPPE). Experimentally, the trans dihedral fraction has been estimated using Raman spectroscopy. Casal and Mantsch[71] determined the central bond in pure liquid C_{13} had a trans fraction of 0.67 (based on a reported 0.33 gauche fraction). Snyder and Kim[72] measured the gauche-trans equilibria of C_4 to C_9 averaged across all C-C bonds, finding a trans fraction of 0.664 (gauche fraction of 0.336) for liquid C_9 at 300 K.

Although nucleation was observed for some force fields, the level of supercooling required was in excess of 40 K in some instances. For example, the TraPPE model which shows the melting point of C_{16} to be 306 K (see Table 7 below) nucleated solid C_{16} at approximately 261 K. When nucleation was observed, solid growth proceeded along the a and b lattice directions, which are perpendicular to the long axis of the molecule. This is consistent with experimental observations of n-alkane crystal growth which find thin rhombic platelets with large (001) faces.[73] In our simulations, these platelets are observed to couple across periodic boundaries to create a frozen layer with no boundary except for the (001) face.

The PYS, MARTINI, L-OPLS and Williams 7/7B force fields did not nucleate solid phase for the default temperature ranges used (340 to 240 K for C_{16}, 330 to 230 K for C_{15}). When reducing these temperature profiles by 5 K and 10 K for C_{15} and C_{16} respectively, nucleation was observed for L-OPLS and Williams 7, but not for PYS, MARTINI and Williams 7B. Reducing by a further 10 K resulted in a solid nucleus forming in the PYS simulation of C_{16}, as predicted by the nucleation probability calculation (Supporting Information Fig. S4), which estimated a 60% chance of observing a supercritical nucleus for this temperature range. Molecular dynamics simulations inevitably require much shorter time scales (tens of ns) and smaller volumes (hundreds of nm^3) than experiment. As the overall nucleation rate is proportional to the volume, simulations require levels of supercooling which would not be observed experimentally. However, diffusion and crystal growth at such low temperatures was slow, and the system did not fully solidify before melting during the heating part of the cycle. Even lower temperatures were not used, as this would slow any crystal growth further

and the system may also solidify as a glass phase.

Williams 7 and 7B had nearly identical trans dihedral fraction in the liquid phase (0.637 and 0.639 respectively at 298 K), so only Williams 7 is shown in Figure 6. As discussed in the next section, the PYS, Williams 7/7B and L-OPLS force fields were found to have the most accurate melting points, so it may be the artificially high melting points of the other models that assists solid nucleation. These force fields (with lower melting points) are characterized by a lower fraction of trans C-C-C-C dihedrals in the liquid phase, highlighting the connection between the conformer populations, which depend on the dihedral potential, and the melting point.

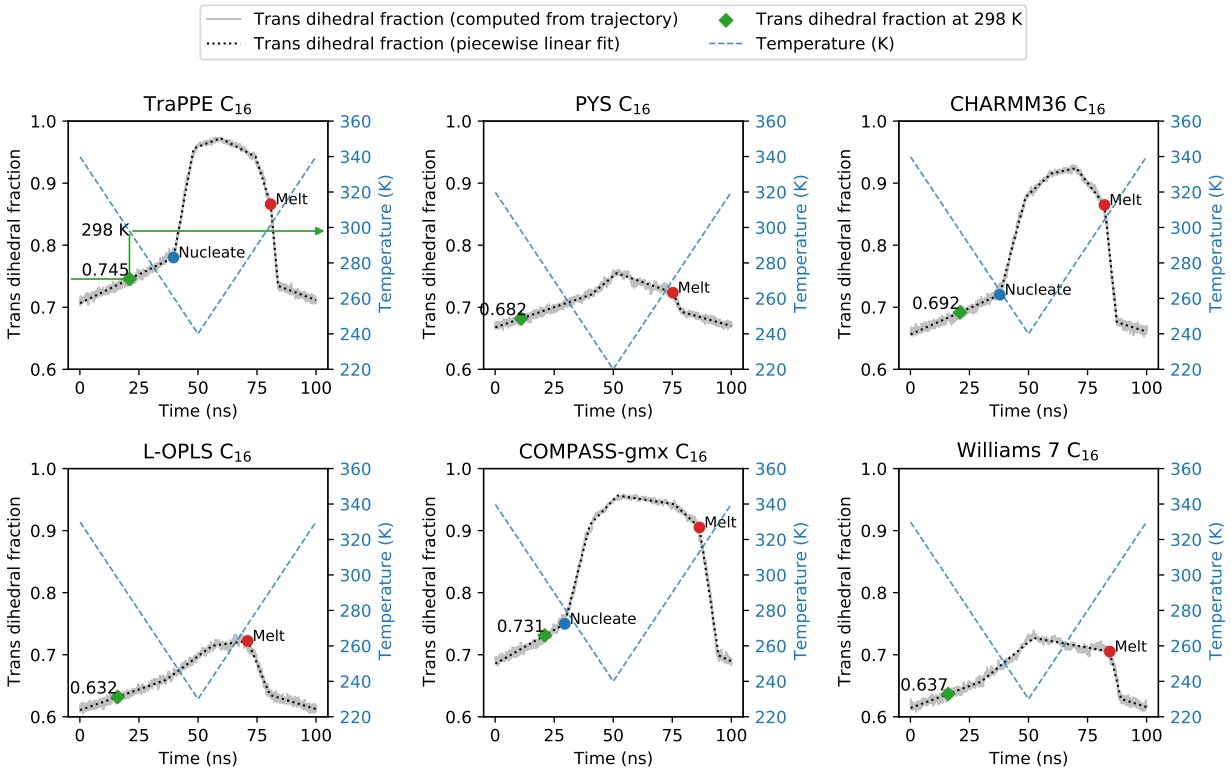

Figure 6: Fraction of C-C-C-C dihedrals in trans conformation for C_{16} during cooling and heating cycle, for each force field. Also shown is the temperature cycle (blue dashed line), the points at which nucleation or melting could be clearly identified (blue and red dots respectively), and the trans dihedral fraction at 298 K (green diamond). The upper left plot illustrates how the temperature is read off the right side y axis.

Computed Melting Points

The planar interface method was found to be a reliable way of measuring the melting point of n-alkanes. Given sufficient time at constant temperature, the change in density became a monotonic function of the simulation temperature, which allows the melting point to be determined unambiguously as the temperature at which the smallest density change is observed. The required time scales were not particularly long, with 10–20 ns at each temperature typically enough to determine whether the system will solidify or melt. An example of this is shown in Figure 7a, which shows the density evolution of the TraPPE model of C_{16}, from which the melting point was determined to be 306 ± 1 K (experimental value 291 K[74]). By contrast, a crystal with a solid-liquid interface perpendicular to the c-axis was not useful for determining the melting point (Figure 7b). The final melting points determined using the planar interface method for all models are given in Table 7 for C_{15} and C_{16}. The PYS force field most closely matched the experimentally observed melting points, with a mean deviation of 2 K, closely followed by Williams 7B (mean deviation of 3 K). Removing the long range dispersion correction for CHARMM36 decreases both melting points by 8 K, increasing the accuracy. The difference between C_{15} and C_{16} melting points was between 6 and 8 K for all force fields, similar to the experimentally observed difference of 8 K.

Order Parameters from Crystal Simulations

We investigated the ability of the different force fields to model solid-solid phase transitions in alkanes, and specifically to reproduce features of rotator phases. The evolution of the order parameters during the heating and cooling cycle of a C_{15} crystal are shown in Figure 8 for each force field. The cycle starts with a 5 ns equilibration at 270 K, followed by a linear 20 ns ramp to 310 K and 20 ns cooling back to 270 K.

The all-atom force fields all showed a transition from herringbone order to parallel order during the 270 K equilibration stage, which was not reversed at any point. This transition

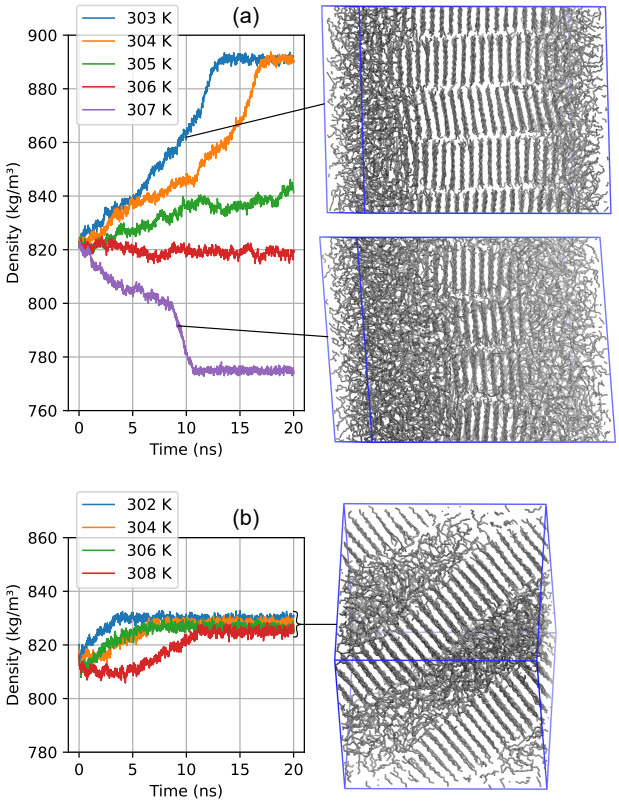

Figure 7: Evolution of average system density of C_{16} using the TraPPE force field, for varying temperatures and two different initial configurations. The upper system (a) has a solid-liquid interface with normal parallel to the a lattice direction of the solid. From the evolution in density, the melting point could be determined to be 306 K. The lower system (b) is sampled from the nucleation study (the nucleation having occurred at a lower temperature) and its interface has normal parallel to the c lattice direction. In this case the system becomes trapped in a solid-liquid configuration which is stable over a wide temperature range, making it impossible to determine the melting point if this initial configuration is used.

Table 7: Melting points of C_{15} and C_{16} for each force field determined by the planar interface method.

Model	Melting point (K) C_{15}	C_{16}
TraPPE	299 ± 1	306 ± 1
PYS	286 ± 1	292 ± 1
CHARMM36	307 ± 1	314 ± 1
CHARMM36 (no DC)[b]	299 ± 1	306 ± 1
L-OPLS	296 ± 1	304 ± 1
COMPASS-gmx	317 ± 1	324 ± 1
Williams 7	294 ± 1	300 ± 1
Williams 7B (this work)	287 ± 1	293 ± 1
MARTINI	-	274 ± 1
Experiment[a]	283.1 ± 0.5	291.2 ± 0.5

[a]Experimental values taken from the review of Dirand et al.[74]

[b]'no DC' denotes CHARMM36 values computed without the long range dispersion correction.

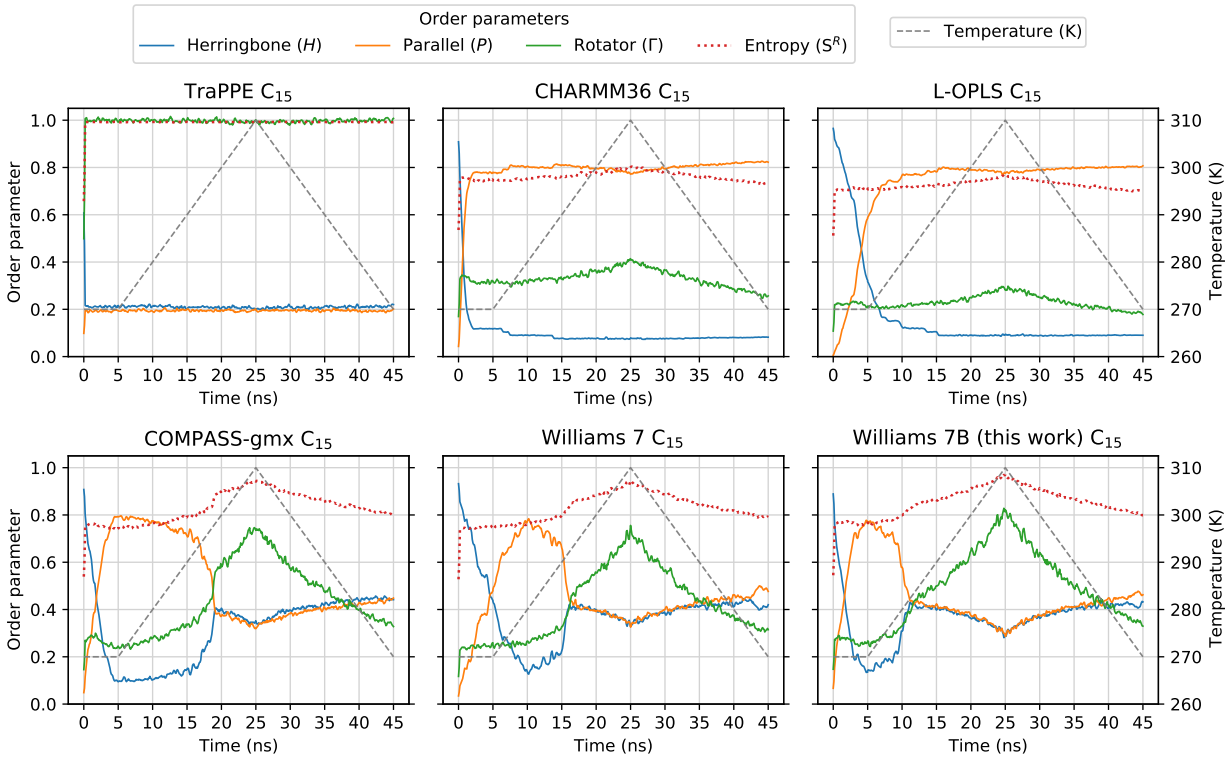

Figure 8: Evolution of crystal and rotator order parameters during heating and cooling cycle of a C_{15} crystal for each force field. The starting configuration is the orthorhombic crystal, and the first 5 ns are at a constant temperature of 270 K. All plots share the same y axis scale, with the temperature (gray dashed line) scale on the rightmost y axis. The PYS force field is not shown as it has nearly identical behavior to TraPPE.

was the fastest for the CHARMM36 force field, taking under 2 ns. An example of this transition for L-OPLS is shown in Figure 9a–9c. The Williams 7/7B force fields continued to demonstrate small regions of herringbone order after this transition, but these were transient. Although this transition to parallel order was consistently observed for all the all-atom force fields, it contradicts experimental observations in which the orthorhombic crystal with herringbone order is the stable structure.

Only the Williams 7/7B and COMPASS-gmx force fields demonstrated a crystal to rotator phase transition for C_{15}, which can be identified by the discontinuous increase in the order parameter Γ, at which point the herringbone and parallel order parameters collapse to the same value. A visualization of this rotator phase is shown in Figure 9d, which can be compared to the perfect herringbone pattern of the orthorhombic crystal in Figure 9a. By examining the change in lattice parameters as the heating continues (Figure S7 provided in Supporting Information), we observe the expected behavior of the R_I phase, in which the lattice parameter a (denoted b by Ungar[63]) increases upon crystal-R_I phase transition then decreases with increasing temperature. The experimentally observed temperature of this crystal to R_I transition is approximately 271 K for C_{15},[63] which is 12 K below the melting point. Here we observe the crystal-R_I transition at approximately 290 K and 279 K for the Williams 7 and 7B force fields respectively, which is 4 K and 8 K below their respective melting points of 294 K and 287 K. Whilst superheating is not observed experimentally for such crystal-rotator transitions,[2] we can not rule out its occurrence in simulations due to the unrealistic heating rates required.

As reported in previous works,[34,40] united-atom force fields will only form a rotationally disordered solid phase. This was true for both TraPPE and PYS, as the Γ and S^R order parameters immediately go to unity when the simulation begins at 270 K, demonstrating a phase with complete rotational disorder and no significantly preferred orientations. With the MARTINI force field, the lamellar solid was stable, but significant displacement of molecules was observed normal to the lamellar layers. This displacement was typically 1/4 of the

lamellar layer spacing, which corresponds to one coarse-grained bond or ≈ 0.5 nm. Since the solid alkane molecules have rod-like geometry with MARTINI, the atoms are nearly colinear and the second principal component (which defines rotation about the long axis of the molecule) is not well defined. Therefore the order parameters are not reported for MARTINI.

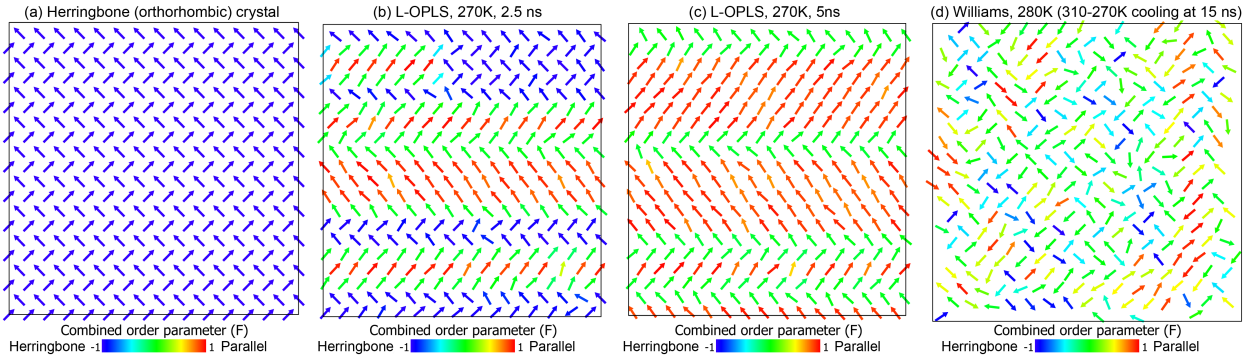

Figure 9: Second principal component vectors, $\boldsymbol{p}_2$, computed for molecules in one layer of a C_{15} crystal. The visualization is produced using Ovito.[75] (a) Starting configuration which is the experimentally observed orthorhombic crystal with herringbone order. (b)-(c) transition from herringbone to mostly parallel order over 5 ns, which is observed at varying rates for all of the all-atom force fields. (d) Rotator phase R_I which is observed only for the Williams and COMPASS-gmx force fields.

For C_{16}, all the all-atom force fields correctly reproduced that C_{16} forms a triclinic phase in which the molecules all share the same orientation and are tilted with respect to the layer normal. The evolution of the rotator order parameters Γ and S^R for C_{16} are given in the Supporting Information Figure S6, and it is seen that only the COMPASS-gmx and the optimized Williams 7B model demonstrate a crystal-rotator phase transition in this case. Although the rotator phase of C_{16} is not found to be stable experimentally, it is still observed as a transient phase[2] or in the presence of an interface.[17]

Computational Performance

A summary of the computational performance of each force field is given in the Supporting Information. The most efficient force field, PYS, was approximately 50 times faster than

the most computationally expensive model (COMPASS-gmx). This dramatic difference is a result of many factors which are advantageous for performance, with the main ones being the united-atom representation, a 2 fs time step compared to 1 fs, a fairly short potential cutoff of 1 nm, the lack of point charges, and use of the 12-6 LJ potential which is highly optimized in GROMACS compared to the tabulated potential used for COMPASS-gmx. In alternative software where tabulation of the 9-6 LJ potential is not necessary, this difference would be reduced. It may also be possible to use a 2 fs time step for all force fields since C-H bonds are constrained, but this would require additional validation. If other components are present in the system, such as water, these may become a computational bottleneck, so there will be less benefit to using a highly efficient alkane model.

Conclusions

Seven different force fields, one of which was a newly optimized Buckingham potential (Williams 7B), were benchmarked by measuring the liquid density, self-diffusion coefficient, melting point, and the solid phase structure as a function of temperature.

It was known that united-atom models form a rotationally disordered solid phase, and we have quantified that the level of rotational disorder is near maximum, as the two rotator order parameters are close to unity for both TraPPE and PYS. Despite this limitation, they remain an attractive option in cases where the rotational order is not thought to be important, due to their much reduced computational cost. United-atom models can still perform well for other properties, as demonstrated by PYS reproducing the melting points of C_{15} and C_{16} to within 1–3 K, with Williams 7B the only other force field with comparable accuracy.

We observed contrasting behaviour between the all-atom 12-6 LJ force fields and those using pair potentials with softer repulsive terms (9-6 LJ and Buckingham). The 12-6 LJ potentials, CHARMM36 and L-OPLS, shared a key behavior in that no rotator phase was

observed for either force field, even when reaching 310 K for C_{15} which is nearly 30 K above its experimentally observed melting point. Further heating of the CHARMM36 C_{15} crystal found a transition to rotational disorder followed immediately by melting at approximately 326 K, so no stable rotator phase was observed. The COMPASS-gmx and Williams 7/7B force fields successfully reproduced the crystal to rotator transition of C_{15}, with the change in lattice parameters characteristic of the R_I phase.

An updated version of the Williams potential (version 7B) was optimized for use with a 1 nm potential cutoff and long range dispersion corrections to energy and pressure. Although fit to reproduce liquid density and self-diffusion coefficients, it also demonstrated improved accuracy for the melting point and crystal-rotator transition temperature.

As the Williams 7B force field is significantly more computationally expensive than PYS, we must consider the situations where the less expensive united-atom force field may not be suitable. Firstly, the mechanical and rheological properties of paraffin waxes are highly relevant to flow assurance of waxy crude oils and the removal of existing wax deposits in pipelines.[8] Recently, Alade et al. have investigated the softening of wax deposits using thermochemical reactions to raise the oil temperature.[76] It is known that the physical properties of the crystal and rotator phases differ, which has been quantified by measurements of the elastic constants and speed of sound.[77] Wang et al. investigated the viscoelastic properties of paraffin wax and found the dynamic moduli were highly temperature dependent in the crystal phase, and dropped by over one order of magnitude upon crystal-rotator transition.[78] Therefore it is important to accurately predict the correct solid phase of paraffin wax in order to study the temperature-dependent softening of waxes.

Additionally, it is known that the heat of fusion (ΔH_f) associated with a rotator-liquid phase transition is less than the total ΔH_f for the crystal-liquid transition. For example, the total ΔH_f for C_{15} is 45.2 kJ/mol, with the rotator-liquid transition contributing 34.6 kJ/mol.[79] If a force field can only reproduce the rotator phase in the solid, even at conditions where it is known to be fully crystalline, ΔH_f may be underestimated. If a force

field incorrectly predicts ΔH_f, it will limit its applicability for studying the energy storage capacity of alkane-based phase change materials.

The benchmarks described in this work can be used to extend future force field validations to cover solid-liquid and solid-solid phase transitions. Whilst alkanes are a typical usage case, the methods are readily applicable to other classes of molecule. The interface method of measuring the melting point[60,62] can be applied to other molecules with known crystal structure, and the required time scales were tens of nanoseconds for n-alkanes, achievable with modern computational resources. The principal component method used to define the molecular orientation is general and need not be restricted to n-alkanes. The proposed order parameters, which are functions of the principal components, can also be used or adapted for other molecules which form lamellar crystals or ordered phases, such as long chain alcohols, fatty acids and triglycerides.[3]

Acknowledgement

We are grateful for funding from the EPSRC fellowship to S.K.S (EP/R028915/1) and for the UK Materials and Molecular Modelling Hub for computational resources, which is partially funded by EPSRC (EP/P020194/1). This research utilised Queen Mary's Apocrita HPC facility, supported by QMUL Research-IT (http://doi.org/10.5281/zenodo.438045). The authors acknowledge the use of the IRIDIS High Performance Computing Facility, and associated support services at the University of Southampton, in the completion of this work.

Supporting Information Available

Archive containing GROMACS force field files; link to online repository (hosted at `https://github.com/sb8`) where updates to these files and additional information can be provided.

Supplementary figures: Trans dihedral fraction during nucleation study of C_{15}; evolution of rotator phase order parameters for C_{16} crystal; change in lattice parameters during crystal-

rotator phase transition of C_{15}. Supplementary tables: Summary of simulation performance for each force field; GROMACS version used for each simulation.

This material is available free of charge via the Internet at `http://pubs.acs.org/`.

References

(1) Sirota, E.; King Jr, H.; Singer, D.; Shao, H. H. Rotator phases of the normal alkanes: An x-ray scattering study. *The Journal of Chemical Physics* **1993**, *98*, 5809–5824.

(2) Sirota, E.; Herhold, A. Transient rotator phase induced nucleation in n-alkane melts. *Polymer* **2000**, *41*, 8781–8789.

(3) Dorset, D. L. *Crystallography of the polymethylene chain: an inquiry into the structure of waxes*; Oxford University Press, 2005; Vol. 17.

(4) Tenchov, B.; Koynova, R.; Rapp, G. New ordered metastable phases between the gel and subgel phases in hydrated phospholipids. *Biophysical Journal* **2001**, *80*, 1873–1890.

(5) Peng, H.; Zhang, D.; Ling, X.; Li, Y.; Wang, Y.; Yu, Q.; She, X.; Li, Y.; Ding, Y. N-alkanes phase change materials and their microencapsulation for thermal energy storage: A critical review. *Energy & Fuels* **2018**, *32*, 7262–7293.

(6) Qiu, X.; Song, G.; Chu, X.; Li, X.; Tang, G. Microencapsulated n-alkane with p(n-butyl methacrylate-co-methacrylic acid) shell as phase change materials for thermal energy storage. *Solar Energy* **2013**, *91*, 212–220.

(7) Cholakova, D.; Denkov, N. Rotator phases in alkane systems: In bulk, surface layers and micro/nano-confinements. *Advances in Colloid and Interface Science* **2019**, *269*, 7–42.

(8) Aiyejina, A.; Chakrabarti, D. P.; Pilgrim, A.; Sastry, M. Wax formation in oil pipelines: A critical review. *International Journal of Multiphase Flow* **2011**, *37*, 671–694.

(9) Holder, G.; Winkler, J. Crystal-growth poisoning of n-paraffin wax by polymeric additives and its relevance to polymer crystallization mechanisms. *Nature* **1965**, *207*, 719–721.

(10) Jang, Y. H.; Blanco, M.; Creek, J.; Tang, Y.; Goddard, W. A. Wax inhibition by comb-like polymers: support of the incorporation-perturbation mechanism from molecular dynamics simulations. *The Journal of Physical Chemistry B* **2007**, *111*, 13173–13179.

(11) Shahruddin, S.; Jiménez-Serratos, G.; Britovsek, G.; Matar, O.; Müller, E. Fluid-solid phase transition of n-alkane mixtures: Coarse-grained molecular dynamics simulations and diffusion-ordered spectroscopy nuclear magnetic resonance. *Scientific Reports* **2019**, *9*, 1–9.

(12) Kralova, I.; Sjöblom, J. Surfactants used in food industry: a review. *Journal of Dispersion Science and Technology* **2009**, *30*, 1363–1383.

(13) Rebello, S.; Asok, A. K.; Mundayoor, S.; Jisha, M. Surfactants: toxicity, remediation and green surfactants. *Environmental Chemistry Letters* **2014**, *12*, 275–287.

(14) Butler, L. N.; Fellows, C. M.; Gilbert, R. G. Effect of surfactants used for binder synthesis on the properties of latex paints. *Progress in Organic Coatings* **2005**, *53*, 112–118.

(15) Stillwell, W. In *An Introduction to Biological Membranes (Second Edition)*, second edition ed.; Stillwell, W., Ed.; Elsevier, 2016; pp 63–87.

(16) Clerc, S. G.; Thompson, T. E. Permeability of dimyristoyl phosphatidylcholine/dipalmitoyl phosphatidylcholine bilayer membranes with coexisting gel and liquid-crystalline phases. *Biophysical Journal* **1995**, *68*, 2333–2341.

(17) Ueno, S.; Hamada, Y.; Sato, K. Controlling polymorphic crystallization of n-alkane crys-

tals in emulsion droplets through interfacial heterogeneous nucleation. *Crystal Growth & Design* **2003**, *3*, 935–939.

(18) Cholakova, D.; Denkov, N.; Tcholakova, S.; Lesov, I.; Smoukov, S. K. Control of drop shape transformations in cooled emulsions. *Advances in Colloid and Interface Science* **2016**, *235*, 90–107.

(19) Denkov, N.; Tcholakova, S.; Lesov, I.; Cholakova, D.; Smoukov, S. K. Self-shaping of oil droplets via the formation of intermediate rotator phases upon cooling. *Nature* **2015**, *528*, 392–395.

(20) Marin, O.; Alesker, M.; Guttman, S.; Gershinsky, G.; Edri, E.; Shpaisman, H.; Guerra, R. E.; Zitoun, D.; Deutsch, M.; Sloutskin, E. Self-faceting of emulsion droplets as a route to solid icosahedra and other polyhedra. *Journal of Colloid and Interface Science* **2019**, *538*, 541–545.

(21) Tcholakova, S.; Valkova, Z.; Cholakova, D.; Vinarov, Z.; Lesov, I.; Denkov, N.; Smoukov, S. K. Efficient self-emulsification via cooling-heating cycles. *Nature Communications* **2017**, *8*, 1–11.

(22) Valkova, Z.; Cholakova, D.; Tcholakova, S.; Denkov, N.; Smoukov, S. K. Mechanisms and control of self-emulsification upon freezing and melting of dispersed alkane drops. *Langmuir* **2017**, *33*, 12155–12170.

(23) Lesov, I.; Valkova, Z.; Vassileva, E.; Georgiev, G. S.; Ruseva, K.; Simeonov, M.; Tcholakova, S.; Denkov, N. D.; Smoukov, S. K. Bottom-up synthesis of polymeric micro-and nanoparticles with regular anisotropic shapes. *Macromolecules* **2018**, *51*, 7456–7462.

(24) Guttman, S.; Kesselman, E.; Jacob, A.; Marin, O.; Danino, D.; Deutsch, M.; Sloutskin, E. Nanostructures, faceting, and splitting in nanoliter to yoctoliter liquid droplets. *Nano Letters* **2019**, *19*, 3161–3168.

(25) Haas, P. A.; Goldstein, R. E.; Smoukov, S. K.; Cholakova, D.; Denkov, N. Theory of shape-shifting droplets. *Physical Review Letters* **2017**, *118*, 088001.

(26) Haas, P. A.; Cholakova, D.; Denkov, N.; Goldstein, R. E.; Smoukov, S. K. Shape-shifting polyhedral droplets. *Physical Review Research* **2019**, *1*, 023017.

(27) Cholakova, D.; Denkov, N.; Tcholakova, S.; Valkova, Z.; Smoukov, S. K. Multilayer formation in self-shaping emulsion droplets. *Langmuir* **2019**, *35*, 5484–5495.

(28) García-Aguilar, I.; Fonda, P.; Sloutskin, E.; Giomi, L. Faceting and Flattening of Emulsion Droplets: A Mechanical Model. *Physical Review Letters* **2021**, *126*, 038001.

(29) Ko, M. J.; Waheed, N.; Lavine, M. S.; Rutledge, G. C. Characterization of polyethylene crystallization from an oriented melt by molecular dynamics simulation. *The Journal of Chemical Physics* **2004**, *121*, 2823–2832.

(30) Venerus, D. C.; Schieber, J. D.; Balasubramanian, V.; Bush, K.; Smoukov, S. Anisotropic thermal conduction in a polymer liquid subjected to shear flow. *Physical Review Letters* **2004**, *93*, 098301.

(31) Striolo, A.; Cole, D. R. Understanding shale gas: Recent progress and remaining challenges. *Energy & Fuels* **2017**, *31*, 10300–10310.

(32) Zheng, Q.; Brown, J. L.; Mantle, M. D.; Sederman, A. J.; Baart, T. A.; Guédon, C. M.; Gladden, L. F. Water-wax behaviour in porous silica at low temperature Fischer-Tropsch conditions. *Applied Catalysis A: General* **2019**, *572*, 142–150.

(33) Schaerer, A.; Busso, C.; Smith, A. t.; Skinner, L. Properties of pure normal alkanes in the C17 to C36 range. *Journal of the American Chemical Society* **1955**, *77*, 2017–2019.

(34) Wentzel, N.; Milner, S. T. Crystal and rotator phases of n-alkanes: A molecular dynamics study. *The Journal of Chemical Physics* **2010**, *132*, 044901.

(35) Wentzel, N.; Milner, S. T. Simulation of multiple ordered phases in C23 n-alkane. *The Journal of Chemical Physics* **2011**, *134*, 224504.

(36) Williams, D. E. Nonbonded potential parameters derived from crystalline hydrocarbons. *The Journal of Chemical Physics* **1967**, *47*, 4680–4684.

(37) Sun, H. COMPASS: An ab initio force-field optimized for condensed-phase applications—overview with details on alkane and benzene compounds. *The Journal of Physical Chemistry B* **1998**, *102*, 7338–7364.

(38) Kulakova, L.; Arampatzis, G.; Angelikopoulos, P.; Hadjidoukas, P.; Papadimitriou, C.; Koumoutsakos, P. Data driven inference for the repulsive exponent of the Lennard-Jones potential in molecular dynamics simulations. *Scientific Reports* **2017**, *7*, 1–10.

(39) Galliéro, G.; Boned, C.; Baylaucq, A.; Montel, F. Molecular dynamics comparative study of Lennard-Jones α-6 and exponential α-6 potentials: Application to real simple fluids (viscosity and pressure). *Physical Review E* **2006**, *73*, 061201.

(40) Ryckaert, J.-P.; Klein, M. L. Translational and rotational disorder in solid n-alkanes: Constant temperature–constant pressure molecular dynamics calculations using infinitely long flexible chains. *The Journal of Chemical Physics* **1986**, *85*, 1613–1620.

(41) Waheed, N.; Ko, M.; Rutledge, G. Molecular simulation of crystal growth in long alkanes. *Polymer* **2005**, *46*, 8689–8702.

(42) Yi, P.; Rutledge, G. C. Molecular simulation of crystal nucleation in n-octane melts. *The Journal of Chemical Physics* **2009**, *131*, 134902.

(43) Yamamoto, T. Molecular dynamics of crystallization in n-alkane mixtures; texture, compatibility, and diffusion in crystals. *Polymer* **2016**, *99*, 721–733.

(44) Panizon, E.; Bochicchio, D.; Monticelli, L.; Rossi, G. MARTINI coarse-grained models

of polyethylene and polypropylene. *The Journal of Physical Chemistry B* **2015**, *119*, 8209–8216.

(45) Siu, S. W.; Pluhackova, K.; Böckmann, R. A. Optimization of the OPLS-AA force field for long hydrocarbons. *Journal of Chemical Theory and Computation* **2012**, *8*, 1459–1470.

(46) Jorgensen, W. L.; Maxwell, D. S.; Tirado-Rives, J. Development and testing of the OPLS all-atom force field on conformational energetics and properties of organic liquids. *Journal of the American Chemical Society* **1996**, *118*, 11225–11236.

(47) Nieto-Draghi, C.; Ungerer, P.; Rousseau, B. Optimization of the anisotropic united atoms intermolecular potential for n-alkanes: Improvement of transport properties. *The Journal of Chemical Physics* **2006**, *125*, 044517.

(48) Abraham, M. J.; Murtola, T.; Schulz, R.; Páll, S.; Smith, J. C.; Hess, B.; Lindahl, E. GROMACS: High performance molecular simulations through multi-level parallelism from laptops to supercomputers. *SoftwareX* **2015**, *1*, 19–25.

(49) Martin, M. G.; Siepmann, J. I. Transferable potentials for phase equilibria. 1. United-atom description of n-alkanes. *The Journal of Physical Chemistry B* **1998**, *102*, 2569–2577.

(50) Smith, G. D.; Yoon, D. Y. Equilibrium and dynamic properties of polymethylene melts from molecular dynamics simulations. I. n-Tridecane. *The Journal of Chemical Physics* **1994**, *100*, 649–658.

(51) Marrink, S. J.; Risselada, H. J.; Yefimov, S.; Tieleman, D. P.; De Vries, A. H. The MARTINI force field: coarse grained model for biomolecular simulations. *The Journal of Physical Chemistry B* **2007**, *111*, 7812–7824.

(52) Klauda, J. B.; Venable, R. M.; Freites, J. A.; O'Connor, J. W.; Tobias, D. J.; Mondragon-Ramirez, C.; Vorobyov, I.; MacKerell Jr, A. D.; Pastor, R. W. Update of the CHARMM all-atom additive force field for lipids: validation on six lipid types. *The Journal of Physical Chemistry B* **2010**, *114*, 7830–7843.

(53) Bussi, G.; Donadio, D.; Parrinello, M. Canonical sampling through velocity rescaling. *The Journal of Chemical Physics* **2007**, *126*, 014101.

(54) Parrinello, M.; Rahman, A. Polymorphic transitions in single crystals: A new molecular dynamics method. *Journal of Applied physics* **1981**, *52*, 7182–7190.

(55) Yeh, I.-C.; Hummer, G. System-size dependence of diffusion coefficients and viscosities from molecular dynamics simulations with periodic boundary conditions. *The Journal of Physical Chemistry B* **2004**, *108*, 15873–15879.

(56) Kowert, B. A.; Sobush, K. T.; Fuqua, C. F.; Mapes, C. L.; Jones, J. B.; Zahm, J. A. Size-dependent diffusion in the n-alkanes. *The Journal of Physical Chemistry A* **2003**, *107*, 4790–4795.

(57) Yi, P.; Rutledge, G. C. Molecular simulation of bundle-like crystal nucleation from n-eicosane melts. *The Journal of Chemical Physics* **2011**, *135*, 024903.

(58) Uhlmann, D. R.; Kritchevsky, G.; Straff, R.; Scherer, G. Crystal nucleation in normal alkane liquids. *The Journal of Chemical Physics* **1975**, *62*, 4896–4903.

(59) Jiang, S.; ter Horst, J. H. Crystal nucleation rates from probability distributions of induction times. *Crystal Growth & Design* **2011**, *11*, 256–261.

(60) Zhang, Y.; Maginn, E. J. A comparison of methods for melting point calculation using molecular dynamics simulations. *The Journal of Chemical Physics* **2012**, *136*, 144116.

(61) Humphrey, W.; Dalke, A.; Schulten, K. VMD – Visual Molecular Dynamics. *Journal of Molecular Graphics* **1996**, *14*, 33–38.

(62) Bai, X.-M.; Li, M. Calculation of solid-liquid interfacial free energy: A classical nucleation theory based approach. *The Journal of Chemical Physics* **2006**, *124*, 124707.

(63) Ungar, G. Structure of rotator phases in n-alkanes. *The Journal of Physical Chemistry* **1983**, *87*, 689–695.

(64) Tu, K.; Tobias, D. J.; Klein, M. L. Constant pressure and temperature molecular dynamics simulations of crystals of the lecithin fragments: glycerylphosphorylcholine and dilauroylglycerol. *The Journal of Physical Chemistry* **1995**, *99*, 10035–10042.

(65) Apr, E.; Bylaska, E. J.; de Jong, W. A.; Govind, N.; Kowalski, K.; Straatsma, T. P.; Valiev, M.; van Dam, H. J. J.; Alexeev, Y.; Anchell, J. et al. NWChem: Past, present, and future. *The Journal of Chemical Physics* **2020**, *152*, 184102.

(66) Hamani, A. W. S.; Bazile, J.-P.; Hoang, H.; Luc, H. T.; Daridon, J.-L.; Galliero, G. Thermophysical properties of simple molecular liquid mixtures: On the limitations of some force fields. *Journal of Molecular Liquids* **2020**, *303*, 112663.

(67) Messerly, R. A.; Anderson, M. C.; Razavi, S. M.; Elliott, J. R. Improvements and limitations of Mie λ-6 potential for prediction of saturated and compressed liquid viscosity. *Fluid Phase Equilibria* **2019**, *483*, 101–115.

(68) Aucejo, A.; Burguet, M. C.; Munoz, R.; Marques, J. L. Densities, viscosities, and refractive indices of some n-alkane binary liquid systems at 298.15 K. *Journal of Chemical and Engineering Data* **1995**, *40*, 141–147.

(69) Daridon, J.-L.; Carrier, H.; Lagourette, B. Pressure dependence of the thermophysical properties of n-pentadecane and n-heptadecane. *International Journal of Thermophysics* **2002**, *23*, 697–708.

(70) Tofts, P.; Lloyd, D.; Clark, C.; Barker, G.; Parker, G.; McConville, P.; Baldock, C.; Pope, J. Test liquids for quantitative MRI measurements of self-diffusion coefficient in

vivo. *Magnetic Resonance in Medicine: An Official Journal of the International Society for Magnetic Resonance in Medicine* **2000**, *43*, 368–374.

(71) Casal, H.; Mantsch, H. Positional dependence of solvent effects on the conformation of liquid n-alkanes. An infrared spectroscopic study. *Journal of Molecular Structure* **1989**, *192*, 41–45.

(72) Snyder, R. G.; Kim, Y. Conformation and low-frequency isotropic Raman spectra of the liquid n-alkanes C4-C9. *The Journal of Physical Chemistry* **1991**, *95*, 602–610.

(73) Camacho, D. M.; Roberts, K. J.; Lewtas, K.; More, I. The crystal morphology and growth rates of triclinic N-docosane crystallising from N-dodecane solutions. *Journal of Crystal Growth* **2015**, *416*, 47–56.

(74) Dirand, M.; Bouroukba, M.; Briard, A.-J.; Chevallier, V.; Petitjean, D.; Corriou, J.-P. Temperatures and enthalpies of (solid+solid) and (solid+liquid) transitions of n-alkanes. *The Journal of Chemical Thermodynamics* **2002**, *34*, 1255–1277.

(75) Stukowski, A. Visualization and analysis of atomistic simulation data with OVITO–the Open Visualization Tool. *Modelling and Simulation in Materials Science and Engineering* **2009**, *18*, 015012.

(76) Alade, O. S.; Hassan, A.; Mahmoud, M.; Al-Shehri, D.; Al-Majed, A. Novel Approach for Improving the Flow of Waxy Crude Oil Using Thermochemical Fluids: Experimental and Simulation Study. *ACS Omega* **2020**, *5*, 4313–4321.

(77) Jimenez, R.; Kruger, J.; Prechtl, M.; Grammes, C.; Alnot, P. Premelting features and acoustic mode softening in the rotator phases of linear telomers: C17H36. *Journal of Physics: Condensed Matter* **1994**, *6*, 10977.

(78) Wang, J.; Calhoun, M. D.; Severtson, S. J. Dynamic rheological study of paraffin wax

and its organoclay nanocomposites. *Journal of Applied Polymer Science* **2008**, *108*, 2564–2570.

(79) Costa, J. C.; Mendes, A.; Santos, L. M. Chain length dependence of the thermodynamic properties of n-alkanes and their monosubstituted derivatives. *Journal of Chemical & Engineering Data* **2018**, *63*, 1–20.

Graphical TOC Entry